The Astrophysical Journal, 974:270 (13pp), 2024 October 20 https://doi.org/10.3847/1538-4357/ad701e

A Model for Eruptive Mass Loss in Massive Stars

Shelley J. Cheng[1,2], Jared A. Goldberg[2], Matteo Cantiello[2,3], Evan B. Bauer[1], Mathieu Renzo[2,4], and Charlie Conroy[1]
[1] Center for Astrophysics | Harvard & Smithsonian, 60 Garden Street, Cambridge, MA 02138, USA; shelley.cheng@cfa.harvard.edu
[2] Center for Computational Astrophysics, Flatiron Institute, 162 5th Avenue, New York, NY 10010, USA
[3] Department of Astrophysical Sciences, Princeton University, Princeton, NJ 08544, USA
[4] Steward Observatory, University of Arizona, 933 N Cherry Avenue, Tucson, AZ 85721, USA
Received 2024 May 20; revised 2024 August 4; accepted 2024 August 12; published 2024 October 16

Abstract

Eruptive mass loss in massive stars is known to occur, but the mechanism(s) are not yet well understood. One proposed physical explanation appeals to opacity-driven super-Eddington luminosities in stellar envelopes. Here, we present a 1D model for eruptive mass loss and implement this model in the MESA stellar evolution code. The model identifies regions in the star where the energy associated with a local super-Eddington luminosity exceeds the binding energy of the overlaying envelope. The material above such regions is ejected from the star. Stars with initial masses of $10-100\,M_{\odot}$ at solar and SMC metallicities are evolved through core helium burning, with and without this new eruptive mass-loss scheme. We find that eruptive mass loss of up to $\sim 10^{-2}\,M_{\odot}\mathrm{yr}^{-1}$ can be driven by this mechanism, and occurs in a vertical band on the H-R diagram between $3.5 \lesssim \log(T_{\rm eff}/\mathrm{K}) \lesssim 4.0$. This predicted eruptive mass loss prevents stars of initial masses $\gtrsim 20\,M_{\odot}$ from evolving to become red supergiants (RSGs), with the stars instead ending their lives as blue supergiants, and offers a possible explanation for the observed lack of RSGs in that mass regime.

Unified Astronomy Thesaurus concepts: Stellar physics (1621); Stellar winds (1636); Stellar evolution (1599)

1. Introduction

Massive stars ($\gtrsim 10\,M_{\odot}$) are important for understanding the evolution and structure of many astrophysical systems. When studying galaxies, massive stars are important since they impact the overall density and movement of matter which alters galaxy structure, dynamics, and evolution (e.g., see review by L. J. Tacconi et al. 2020). Additionally, mass loss from massive stars and their explosions play an important role in galaxy feedback (e.g., T. M. Heckman et al. 1990; D. Ceverino & A. Klypin 2009; S. Geen et al. 2015; U. P. Steinwandel & J. A. Goldberg 2023). At smaller scales, quantifying the intrinsic mass loss from massive stars can help constrain the masses of compact objects (K. Belczynski et al. 2010; M. Dominik et al. 2012; M. Renzo et al. 2017; S. Banerjee et al. 2020; T. J. Moriya & S.-C. Yoon 2022; T. Fragos et al. 2023), study gravitational wave sources (B. M. Ziosi et al. 2014; M. Mapelli 2016; H. Uchida et al. 2019; J. S. Vink et al. 2021), and better understand the circumstellar environment responsible for observed signatures of interaction in early-time supernova emission (e.g., E. M. Schlegel 1990; A. Pastorello et al. 2007; V. Morozova et al. 2017; R. J. Bruch et al. 2023; W. V. Jacobson-Galán et al. 2024).

Observationally, massive stars are known to exhibit high levels of intrinsic mass loss (e.g., P. R. Wood et al. 1983, 1992; G. Meynet & A. Maeder 2003; N. Smith 2014). In single massive stars, mass loss can generally occur in three ways: a radiation-driven wind, a pulsation-induced dust-driven wind, and through eruptions. One of the first analytical radiation-driven wind models was the CAK model (J. I. Castor et al. 1975), which predicted a mass-loss rate on the order of $10^{-6}\,M_{\odot}\mathrm{yr}^{-1}$ for an O5-type main-sequence star. The CAK model describes how the forces due to metal line absorption of photons can produce a mass outflow, and predicts mass-loss rates and wind terminal velocities (see, e.g., S. P. Owocki et al. 1988; H. J. G. L. M. Lamers & J. P. Cassinelli 1999; N. Smith 2014; M. Cure & I. Araya 2023). While the mass-loss rate predictions of CAK were in general agreement with observations (C. de Jager et al. 1988; H. Nieuwenhuijzen & C. de Jager 1990; T. Nugis & H. J. G. L. M. Lamers 2000), the emissivity of the recombination processes that form emission lines depends on the square of density, so small density inhomogeneities or "clumps" in the wind can cause an overprediction of mass-loss rates if they are not properly modeled. Subsequent work by D. F. Figer et al. (2002), P. A. Crowther et al. (2002), D. J. Hillier et al. (2003), D. Massa et al. (2003), C. J. Evans et al. (2004), J. Puls et al. (2006), E. R. Beasor & B. Davies (2018), and E. R. Beasor et al. (2020) have determined that CAK-based mass-loss rates should be reduced by a factor of 2–10 (P. A. Crowther et al. 2002; D. J. Hillier et al. 2003; A. W. Fullerton et al. 2006; J. Puls et al. 2008; N. Smith 2014).

Pulsation-induced dust-driven winds are likely associated with red supergiants (RSGs) and asymptotic giant branch stars, where atmospheric shock waves caused by stellar pulsations—and possibly convection—are thought to lift gas to low enough temperatures to form dust, which then collisionally couples with photons and accelerates outward as a wind (e.g., L. A. Willson 2000; J. T. van Loon et al. 2005; S. Liljegren et al. 2016; J. A. Goldberg et al. 2022; A. Chiavassa et al. 2024). Observations have suggested wind mass-loss rates of up to $10^{-3}\,M_{\odot}\mathrm{yr}^{-1}$ in RSGs (J. T. van Loon et al. 2005), but mass-loss rates for RSGs are highly uncertain (N. Smith 2014) and potentially overestimated (e.g., E. R. Beasor et al. 2020, 2023; L. Decin et al. 2024). Many common prescriptions assume dust-enshrouded RSGs with higher mass-loss rates (e.g., C. Georgy et al. 2012; S. Ekström et al. 2012; S. R. Goldman

et al. 2017), and the choice of mass-loss model can significantly alter the evolutionary track of an RSG, with lower mass-loss rates allowing the star to remain in the red but higher mass-loss rates driving the star toward the blue (N. Smith 2014; M. Renzo et al. 2017; E. R. Beasor & B. Davies 2018; E. R. Beasor et al. 2020; J. Josiek et al. 2024) after spending time in the RSG phase. Observationally, RSGs exhibit an (apparent) maximum luminosity of $\log(L/L_{\odot}) \approx 5.5$, which corresponds to a maximum initial mass of around $20-30\,M_{\odot}$ (P. Massey et al. 2000; A. Heger et al. 2003; E. M. Levesque et al. 2009; S. Ekström et al. 2012; T. Z. Dorn-Wallenstein et al. 2023). Post-main-sequence mass loss has been suggested as a possible theory explaining this, particularly involving stars that exceed the Eddington luminosity limit (e.g., J. Puls et al. 2008). However, the specific nature of this mass loss is not well understood, and the physical mechanism causing the dearth of RSGs above $20-30\,M_{\odot}$ remains an open problem. Alternative explanations other than eruptive mass loss include envelope inflation (e.g., D. Sanyal et al. 2015, 2017) and binary interactions (e.g., N. Smith 2014; V. Morozova et al. 2015; R. Margutti et al. 2017).

At even higher masses, luminous blue variables (LBVs) have shown very high mass-loss rates of up to $0.1-5\,M_{\odot}\mathrm{yr}^{-1}$ (R. M. Humphreys & K. Davidson 1984; N. Smith 2017). This high rate of mass loss seen in LBVs is observed to only occur for a short period of time, and as such, is referred to as "eruptive massive loss." Despite a few pioneering theoretical works (e.g., S. P. Owocki et al. 2004; N. Smith & S. P. Owocki 2006), efforts to form a comprehensive model for mass loss of massive stars have traditionally focused on developing scaling formulae based on empirical rates (e.g., C. de Jager et al. 1988; H. Nieuwenhuijzen & C. de Jager 1990; J. S. Vink et al. 2001; J. T. van Loon et al. 2005). Additionally, N. Mauron & E. Josselin (2011) and M. Renzo et al. (2017) compare these scaling formulae for solar-metallicity nonrotating stars between $15-35\,M_{\odot}$. However, these steady wind mass-loss schemes do not attempt to and cannot reproduce the high rates of observed eruptive massive loss. Therefore, there has been some work that scales and tunes the theoretical wind mass-loss schemes using observations to reproduce observed rates of mass loss (e.g., S. Ekström et al. 2012; L. Dessart et al. 2013; G. Meynet et al. 2015; J. S. Vink & G. N. Sabhahit 2023). However, these schemes do not provide a physically motivated model that self-consistently captures the effect of eruptive mass loss.

In this work, we begin with an overview of existing literature on radiation-pressure-dominated envelopes of massive stars from one-dimensional (1D) and three-dimensional (3D) models that motivate our work (Section 2). We then develop an energy-based model for eruptive mass loss and implement it within the 1D stellar evolution software MESA (Section 3), and apply our model to massive stars of differing masses (between 10 and $100\,M_{\odot}$) and metallicities (at $0.2\,Z_{\odot}$ and $1\,Z_{\odot}$). We explore the predicted rate of eruptive mass loss (Section 4), and finally discuss our interpretation of our results and conclude in Section 5.

2. Radiation-pressure-dominated Envelopes of Massive Stars

Energy is transported in stars primarily through radiative diffusion and convection, including in the radiation-pressure-dominated extended outer regions of massive star envelopes, where both mechanisms are present. Due to opacity peaks in the envelope (from the recombination of ions of iron, helium, and hydrogen), the local radiative luminosity may exceed the Eddington limit in layers of the envelope below sub-Eddington regions (Y.-F. Jiang et al. 2015, 2018). Therefore, in these envelopes, density and gas pressure inversions may occur, which are thought to contribute to outburst-like "eruptive mass loss" (P. C. Joss et al. 1973; R. M. Humphreys & K. Davidson 1994; B. Paxton et al. 2013). Specifically, the gas pressure increases outward when radiative luminosity is super-Eddington (when $L_{\mathrm{rad}} > L_{\mathrm{Edd}}$), and under specific conditions, a density inversion may occur even if gas pressure is not inverted; see P. C. Joss et al. (1973) and B. Paxton et al. (2013) for more details.

The envelopes of massive stars therefore present both physical and numerical challenges due to the presence of inversions and super-Eddington radiative luminosity. 1D numerical treatments can fail to find a hydrostatic equilibrium solution in these challenging regions (e.g., B. Paxton et al. 2013). This is the case when using mixing-length theory (MLT; e.g., E. Böhm-Vitense 1958; J. P. Cox & R. T. Giuli 1968) or even time-dependent 1D formulations (e.g., R. Kuhfuss 1986; A. S. Jermyn et al. 2023). Realistic 3D simulations show the limits of the 1D treatment, stressing the importance of the interplay between radiative transport and the complex landscape of turbulent fluctuations in the stellar envelope (Y.-F. Jiang et al. 2015). However, these calculations are computationally very expensive, which has prevented a detailed study of the full parameter space relevant to massive stars.

In the stellar evolution code MESA used in this work, several modifications to MLT aimed at these regions in the envelopes of massive stars are available, namely, MLT++ (B. Paxton et al. 2013) and an implicit method (use_superad_reduction; A. S. Jermyn et al. 2023). These methods involve artificially enhancing the efficiency of convection by reducing the superadiabaticity ($\nabla - \nabla_{\mathrm{ad}}$) in regions nearing the Eddington limit, which usually helps the code find a hydrostatic equilibrium solution. The first of these methods, MLT++, was introduced in B. Paxton et al. (2013). While MLT++ allowed the evolution of massive stars to core-collapse, it leads to different efficiencies of energy transport in radiation-dominated stellar envelopes, and the resulting evolution differs from that of convective energy transport by MLT. Subsequently, an implicit method was introduced in A. S. Jermyn et al. (2023) that produces more local and robust results in closer agreement to that from MLT compared to MLT++ (when comparing evolutionary tracks on the H-R diagram from the main sequence to RSG phase, see Figure 17 in Section 7.2 of A. S. Jermyn et al. 2023). Nevertheless, while these 1D recipes can help improve numerical convergence and evolve massive stars further, they are not directly physically motivated.

Mass loss in massive stars has also been studied using 3D radiation-hydrodynamics (RHD) models. Indeed, 3D RHD models find enhanced convection in these radiation- and turbulent-pressure-dominated envelopes (e.g., Y.-F. Jiang et al. 2015, 2018; W. C. Schultz et al. 2023). Y.-F. Jiang et al. (2015) and Y.-F. Jiang et al. (2018) simulated the envelope of massive stars at specific points in their evolution, and determined that nonsteady mass-loss outbursts potentially consistent with LBVs can be driven by helium and iron opacity peaks. Their predicted mass-loss rates are significantly lower than those inferred from

observations (R. M. Humphreys & K. Davidson 1984; N. Smith 2017), possibly due to the fact that line driving and dust formation are not included in the models. The importance of helium and iron opacity peaks in mediating continuum-opacity-driven mass loss is not surprising, as the dependence of opacity on temperature and density near opacity peaks can lead to radiation hydrodynamic instabilities (K. H. Prendergast & E. A. Spiegel 1973; M. Kiriakidis et al. 1993; O. Blaes & A. Socrates 2003; A. Suárez-Madrigal et al. 2013).

As photons carrying energy diffuse outward through the envelopes, they may encounter regions where photon diffusion occurs on a faster timescale than dynamical, convective, and acoustic processes (radiatively inefficient convection). This occurs at optical depths lower than the critical value $\tau_{\rm crit} \equiv c/c_{\rm s}$ (e.g., Y.-F. Jiang et al. 2015), where c is the speed of light and $c_{\rm s}$ is the sound speed. This can also be derived from balancing the diffusive radiation flux and the maximum convective flux in the radiation-pressure-dominated regime (for more details, see Y.-F. Jiang et al. 2015). This definition of critical optical depth is equivalent to the more general definition presented by A. S. Jermyn et al. (2022) (see also discussions in Sections 2 and 4.4 of J. A. Goldberg et al. 2022).

The role of $\tau_{\rm crit}$ in determining convective regions where radiation nonetheless carries significant flux (often termed radiatively inefficient, or sometimes just "inefficient" convection) has been demonstrated in 3D simulations. In particular, Y.-F. Jiang et al. (2015) simulated the radiation-dominated envelopes of massive stars in a plane parallel geometry and found that in certain regions close to the surface of the star more shallow than a critical optical depth $\tau < \tau_{\rm crit}$, convection is unable to carry the super-Eddington flux at the iron opacity peak (which is convectively unstable and locally super-Eddington). When $\tau \gg \tau_{\rm crit}$, convection is efficient (in the radiative sense), with the averaged radiation advection flux consistent with the calculation of convection flux following MLT and sub-Eddington radiative acceleration. In contrast, radiation carries non-negligible flux for $\tau < \tau_{\rm crit}$, and a very significant fraction of the flux for $\tau \ll \tau_{\rm crit}$, despite the convective motion. Even while $\tau \ll \tau_{\rm crit}$, the envelope continues to behave in a turbulent and non-stationary manner, with shocks forming and driving large changes in density, and density inversions dissipating (due to convection) and reforming cyclically. The density inversion at the iron opacity peak is ultimately retained in the time-averaged density profile and the radiative acceleration is larger than the gravitational acceleration, creating an unbinding effect, though a mass-loss or mass-loss rate estimate was unable to be determined since the simulation neglected line driving and the global stellar geometry.

Y.-F. Jiang et al. (2018) simulated large wedges of radiation-dominated envelopes in spherical geometry, and also explored different regions of the H-R diagram compared to Y.-F. Jiang et al. (2015). They found that a convective instability at the iron opacity peak can lead to the formation of a strong helium opacity peak. Upon formation, the helium opacity peak causes local radiative acceleration to exceed the gravitational acceleration by an order of magnitude, leading to most of the overlaying mass being unbound and thereby triggering an outburst up to an instantaneous mass-loss rate of up to $0.05\,M_\odot\,{\rm yr}^{-1}$ (which is still $\sim$10−100 times smaller than observed by, e.g., N. Smith 2014). Additionally, after the envelope has settled into a steady state, convection causes large envelope oscillations during which mass is lost at a rate of $\approx 5 \times 10^{-6}\,M_\odot\,{\rm yr}^{-1}$.

Here, instead of enhancing energy transport artificially as in MLT++ (B. Paxton et al. 2013) and the implicit method (A. S. Jermyn et al. 2023), we introduce a 1D model that converts local super-Eddington radiative luminosity into an average global outflow and explore the effect of this mass loss on stellar evolution.

3. Methods

3.1. MESA

We used `MESA` version `r23.05.1` (B. Paxton et al. 2011, 2013, 2015, 2018, 2019; A. S. Jermyn et al. 2023) to evolve stars between the masses of 10 and $100\,M_\odot$ (at every $1\,M_\odot$ mass increment) at $1\,Z_\odot = 0.0142$ (following G. Houdek & D. O. Gough 2011; M. Asplund et al. 2021) and $0.2\,Z_\odot$ (SMC metallicity). We used the N. Grevesse & A. J. Sauval (1998) metallicity abundance ratios (rescaled to $Z_\odot = 0.0142$), and the `approx21.net` nuclear network (F. X. Timmes 1999). Non-rotating models were allowed to evolve from the pre-main sequence until the end of core helium burning (defined as central helium less than a mass fraction of 10^{-4}). All models evolve through core helium ignition, but due to the aforementioned numerical issues (see Section 2), not all models reach the end of core helium burning.

For convection, we used the MLT treatment following J. P. Cox & R. T. Giuli (1968) with an $\alpha_{\rm MLT}$ of 1.73 following S. Jones et al. (2013) and Y. Li et al. (2019) based on fits to the Sun (R. Trampedach & R. F. Stein 2011). We account for convective overshooting (F. Herwig 2000; B. Paxton et al. 2011) with a combination of step and exponential overshooting for, respectively, the top of the hydrogen burning core (`overshoot_f` =0.345 and `overshoot_f0` =0.01) and the top of all other convective cores (`overshoot_f` =0.01 and `overshoot_f0` =0.005). This closely follows the setup used to produce Figure 18 in Section 7.2 of A. S. Jermyn et al. (2023). Our inlists are provided at this repository: doi:10.5281/zenodo.13306749.

The `MESA` equation of state (EOS) combines OPAL (F. J. Rogers & A. Nayfonov 2002), SCVH (D. Saumon et al. 1995), FreeEOS (A. W. Irwin 2004), HELM (F. X. Timmes & F. D. Swesty 2000), PC (A. Y. Potekhin & G. Chabrier 2010), and Skye (A. S. Jermyn et al. 2021) EOSes. Radiative opacities combine OPAL (C. A. Iglesias & F. J. Rogers 1993, 1996) and data from J. W. Ferguson et al. (2005) and J. Poutanen (2017). Electron conduction opacities are from S. Cassisi et al. (2007). Nuclear reaction rates are from JINA REACLIB (R. H. Cyburt et al. 2010), NACRE (C. Angulo et al. 1999) and G. M. Fuller et al. (1985), T. Oda et al. (1994), and K. Langanke & G. Martınez-Pinedo (2000). Screening is included via the prescription of A. I. Chugunov et al. (2007). Thermal neutrino loss rates are from N. Itoh et al. (1996).

3.2. Mass-loss Model

In `MESA`, mass loss is implemented through wind mass-loss schemes. We employ `MESA`'s "`Dutch`" prescription for $T_{\rm eff} > 4000$ K, which combines the models of J. S. Vink et al. (2001) and T. Nugis & H. J. G. L. M. Lamers (2000) as described in E. Glebbeek et al. (2009) and captures the mass-loss rate due to line-driven stellar winds $\dot{M}_{\rm wind}$. For $T_{\rm eff} < 4000$ K, we adopt the more recent empirical mass-loss

rates of RSGs from L. Decin et al. (2024). This replaces the C. de Jager et al. (1988) or H. Nieuwenhuijzen & C. de Jager (1990) mass-loss rates typically used in MESA's "Dutch" prescription which are considered to overestimate mass-loss rates (see Section 1). The strength of the Dutch wind is modulated by the Dutch_scaling_factor, which is uncertain. We choose a Dutch_scaling_factor of 0.8 (following, e.g., E. Glebbeek et al. 2009; C. E. Fields & S. M. Couch 2021; A. W. Pereira et al. 2024; C. Johnston et al. 2024; S. Shiber et al. 2024) throughout our evolution.

To account for eruptive mass loss, we create a model based on the following energy argument (see also Section 2). Motivated by Y.-F. Jiang et al. (2015), we define the transition between convectively inefficient ($\tau < \tau_{\rm crit}$) and convection-dominated ($\tau > \tau_{\rm crit}$) energy transport at a critical optical depth $\tau_{\rm crit}$:

$$\tau_{\rm crit} \equiv \frac{c}{c_{\rm s}}, \tag{1}$$

where $c_{\rm s}$ is the total sound speed. This is similar to Equation 1 in Y.-F. Jiang et al. (2015), except we adopt the total sound speed rather than the gas isothermal sound speed as a conservative estimate[5] for the effective energy transport by dynamical processes. The critical optical depth $\tau_{\rm crit}$ can be found by equating the photon diffusion timescale and the acoustic timescale for a radial distance Δr in the star, for which

$$\text{acoustic timescale} = \frac{\Delta r}{c_s} \tag{2}$$

$$\text{photon diffusion timescale} = \frac{\Delta r}{c/\tau}, \tag{3}$$

where c_s, Δr, and τ are local values of, respectively, total sound speed, radial distance, and optical depth. Thus, $\tau_{\rm crit}$ is a local value determined at every radius. In the stellar envelope, $\tau = \tau_{\rm crit}$ is only true at one point since both c_s and τ are monotonic functions, and therefore $\tau = \tau_{\rm crit}$ defines a unique location above which $\tau < \tau_{\rm crit}$ everywhere in the outer envelope.

We also follow Y.-F. Jiang et al. (2015) and Y.-F. Jiang et al. (2018)'s interpretation of the balance between radiative acceleration and gravitational acceleration in driving outbursts of mass loss. Specifically, in the $\tau < \tau_{\rm crit}$ region, convection transports the convective luminosity $L_{\rm conv}$, and radiative diffusion transports the radiative luminosity $L_{\rm rad}$, but only up to the Eddington limit $L_{\rm Edd}$, defined as

$$L_{\rm Edd} = \frac{4\pi G c M_{\rm enc}}{\kappa}, \tag{4}$$

with $M_{\rm enc}$ and $\kappa(r)$ being, respectively, the enclosed mass and local opacity.

For any locally super-Eddington radiative luminosity (i.e., for any $L_{\rm rad}$ exceeding $L_{\rm Edd}$), we regard the excess radiative luminosity above $L_{\rm Edd}$ as available to do work to unbind the envelope and contribute to eruptive mass loss. More formally, since photons are able to couple with matter when $\tau \gtrsim 2/3$, the $2/3 \lesssim \tau < \tau_{\rm crit}$ region is of interest if the Eddington limit is locally exceeded by the radiative luminosity. In this case, the photons in the radiatively super-Eddington regions in $2/3 \lesssim \tau < \tau_{\rm crit}$ can energetically couple with matter and drive mass loss. Therefore, we consider any excess radiative luminosity above Eddington ($L_{\rm excess} = L_{\rm rad} - L_{\rm Edd} > 0$) in regions of the stellar model with $\tau < \tau_{\rm crit}$ as available to drive mass loss. The ratio of the radiative, convective, and total luminosity to the Eddington luminosity can be expressed as $\Gamma_{\rm Edd,\ rad} = L_{\rm rad}/L_{\rm Edd}$, $\Gamma_{\rm Edd,\ conv} = L_{\rm conv}/L_{\rm Edd}$, and $\Gamma_{\rm Edd,\ tot} = L_{\rm tot}/L_{\rm Edd}$, respectively.

We choose to adopt the local dynamical time $t_{\rm dyn}$ since eruptive mass loss must be dynamical to define a local excess energy $E_{\rm excess}$ as

$$E_{\rm excess} = E_{\rm excess}(r) = L_{\rm excess} t_{\rm dyn}, \tag{5}$$

where $t_{\rm dyn}$ is

$$t_{\rm dyn} = t_{\rm dyn}(r) = \sqrt{\frac{r^3}{Gm(r)}}, \tag{6}$$

and r and $m(r)$ are, respectively, the radius and mass coordinates. $E_{\rm excess}$ is a local value at each radius r of the star.

For $\tau < \tau_{\rm crit}$, we find the total excess energy at every radius r from

$$E_{\rm tot,\ excess} = E_{\rm tot,\ excess}(r) = \frac{\int_{m(r(\tau_{\rm crit}))}^{m(r)} E_{\rm excess}\ dm}{\int_{m(r(\tau_{\rm crit}))}^{m(r)} dm}. \tag{7}$$

This total excess energy is a cumulative integral from $\tau_{\rm crit}$ outward, and represents a mass average of the excess energy in the super-Eddington region. $E_{\rm tot,\ excess}$ has a value at every radius r up to the surface and is only defined for $\tau < \tau_{\rm crit}$, since this is the only region we consider as possibly able to drive mass loss (see Section 2). We note that the meshing in MESA is very close to uniform in the region of interest ($\tau < \tau_{\rm crit}$), which renders the weighting effectively irrelevant.

We compare this total excess energy with the gravitational binding energy of the overlaying material, which for the mass external to radius r is expressed as

$$E_{\rm bind} = E_{\rm bind}(r) = -\int_{m(r)}^{M} \frac{Gm}{r} dm, \tag{8}$$

for which G is the gravitational constant, m and r are the local mass and radius, dm is the local mass increment in question (at radius r), and M is the mass at the surface (total mass). We conservatively choose not to include other sources of energy, such as thermal energy, recombination energy, and kinetic energy, which are all positive energies that decrease $E_{\rm bind}$. Thus, we expect our estimated eruptive mass-loss rates to be conservative.

For every radius r where $\tau < \tau_{\rm crit}$, we define a local energy difference between the binding energy and the total excess energy as

$$E_{\rm diff} = E_{\rm diff}(r) = E_{\rm tot,\ excess} - |E_{\rm bind}|. \tag{9}$$

We find the innermost radius $r_{\rm mass\ loss}$ greater than the radius of $\tau_{\rm crit}$ above which $E_{\rm diff} > 0$, and then find the difference between the surface mass M and the mass at $r_{\rm mass\ loss}$ to give ΔM. This can be expressed as

$$\Delta M = M - m(r_{\rm mass\ loss}), \tag{10}$$

[5] $c_{\rm s} > c_{\rm gas,\ isothermal}$, so $\tau_{\rm crit}$ used here is smaller and therefore more conservative.

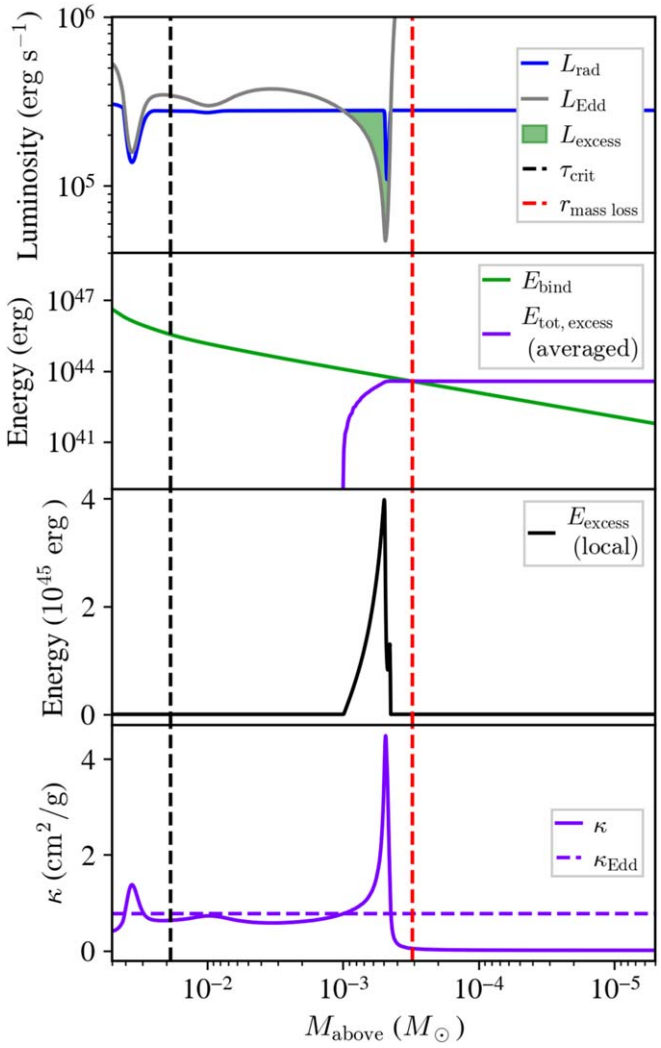

Figure 1. Profiles of luminosity, energy, and opacity as a function of mass above each radius for a $M_{\rm ZAMS} = 30\,M_\odot$, $Z = 1\,Z_\odot$ star. The model chosen corresponds to the time when $\log T_{\rm eff}/{\rm K} = 3.76$, $\log L/L_\odot = 5.45$ on the H-R diagram just after the start of core helium burning (center helium mass fraction of 0.98). For all panels, the horizontal axis is defined as $M_{\rm above} = M - m(r)$. The dashed black and red lines, respectively, show $\tau_{\rm crit}$ and $r_{\rm mass\ loss}$ as defined in Equations (1) and (11). The x-intercept of the red dashed line shows the total mass lost (see Equation (10)). Top panel: local radiative, Eddington (Equation (4)), and excess luminosities. Second panel: total excess energy (Equation (7)) and binding energy (Equation (8)). Third panel: local excess energy (Equation (5)). Last panel: local opacity, showing the opacity peak at around $M_{\rm above} \approx 4 \times 10^{-4}\,M_\odot$ due to both hydrogen and helium ionization transitions.

where

$$r_{\rm mass\ loss} \equiv \min(r) > r(\tau_{\rm crit}) \quad \text{for which} \quad E_{\rm diff} > 0. \tag{11}$$

We emphasize that, at each time step, $E_{\rm bind}$, $E_{\rm tot,\ excess}$, and $E_{\rm diff}$ are functions of radius r. We show how local luminosities (radiative, Eddington, and excess), local excess energy, and total excess energy (a cumulative integral) are accounted for when determining mass loss for our model in Figure 1, which shows a representative model of a $M_{\rm ZAMS} = 30\,M_\odot$ and $Z = 1\,Z_\odot$ star with mass loss due to a hydrogen/helium opacity peak (also shown in the left panel of Figure 2). Figure 2 shows examples of how the opacity peaks (lower panels) can cause the star's radiative luminosity to locally exceed the Eddington limit (green line in top panels).

Finally, we define the mass-loss rate as

$$\dot{M}_{\rm erupt} = \xi \frac{\Delta M}{t_{\rm dyn,\ local}}, \tag{12}$$

where ξ is a free parameter we introduce to tune our model. $t_{\rm dyn,\ local}$ is the local dynamical time at $r_{\rm mass\ loss}$; this is the local dynamical time at the smallest radius in the star for which both $E_{\rm tot,\ excess} > |E_{\rm bind}|$ (where the purple line exceeds the green line in the second panel of Figure 1) and $\tau < \tau_{\rm crit}$ (to the right of the dashed black line in Figure 1). We explore two values of ξ in our modeling; $\xi = 0.1$ and $\xi = 1.0$.

For our total mass-loss model, we combine the wind mass-loss model with our novel eruptive mass-loss model:

$$\dot{M} = \dot{M}_{\rm erupt} + \dot{M}_{\rm wind}. \tag{13}$$

This mass-loss model is implemented as a custom hook in `run_star_extras.f90` and is calculated at each time step of a star's evolution. We note that although no explicit metallicity dependence is included in our eruptive mass-loss model, the mass-loss rate is expected to be indirectly impacted by changes in stellar structure due to metallicity (e.g., C. Xin et al. 2022) such as the effective temperature as well as the depth and strength of the helium and iron opacity peaks.

Using this model, we find that our eruptive mass-loss model behaves as expected; mass loss occurs due to locally super-Eddington radiative luminosity at the hydrogen/helium and iron opacity peaks. As shown in Figure 2, these opacity peaks occur in the $\tau < \tau_{\rm crit}$ region (left of the red dashed line). In particular, the radiative luminosity (marked in green lines and denoted by $\Gamma_{\rm Edd,\ rad}$) can be locally super-Eddington (above the black dashed line) and correspond to the locations of opacity peaks. This locally super-Eddington radiative luminosity can drive eruptive mass loss and, when $\dot{M}_{\rm erupt}$ is sufficiently large, can alter the structure of the star by preventing the formation of an outer convective envelope.

4. Results

In this section, we show our results for eruptive mass loss. Figure 3 presents Kippenhahn diagrams (mass profile over time) of stars modeled with and without eruptive mass loss in addition to stellar winds. As shown in the green hatches in the bottom panel for the star modeled without eruptive mass loss, a convective H-rich envelope is present above the helium-burning region. However, for the model with eruptive mass loss, this convective layer never forms due to eruptive mass loss at 6.3 Myr (in agreement with A. Schootemeijer et al. 2024).

Figure 4 more clearly shows the timing of this eruptive mass loss by presenting the mass-loss rates due to stellar winds and eruptive mass loss over time, as well as the relative importance of $\dot{M}_{\rm erupt}$ compared to $\dot{M}_{\rm wind}$. We see that the mass loss at around 6.3 Myr is indeed primarily due to eruptive mass loss, with $\dot{M}_{\rm erupt}$ exceeding $\dot{M}_{\rm wind}$ by 2 orders of magnitude.

As a result of this eruptive mass loss, the convective layer is not formed and the star no longer evolves cool enough to become a RSG. This can be seen in Figure 5, which shows the evolutionary tracks of the two stars featured in Figure 3 on an H-R diagram. For the model with eruptive mass loss (in purple), the star remains hotter throughout its evolution and does not evolve to become an RSG. This is contrasted with the model with only stellar winds (in green), which evolves cooler

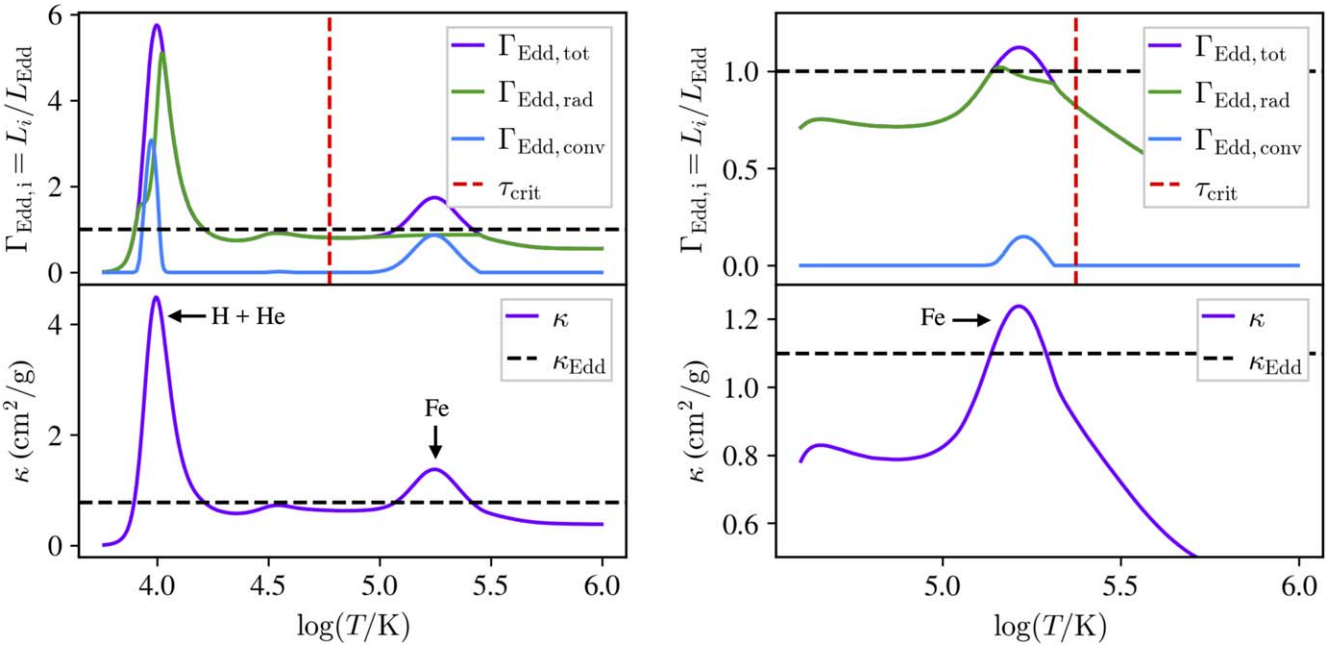

Figure 2. Stellar temperature profiles showing locally super-Eddington radiative luminosity due to opacity peaks. Left panels: a $M_{\rm ZAMS} = 30\,M_\odot$, $Z = 1\,Z_\odot$ model with a opacity peak due to both hydrogen and helium ionization transitions. Left panels correspond to time when $\log T_{\rm eff}/{\rm K} = 3.76$, $\log L/L_\odot = 5.45$ on the H-R diagram. Right panels: a $M_{\rm ZAMS} = 60\,M_\odot$, $Z = 1\,Z_\odot$ model with an iron opacity peak. Right panels correspond to time when $\log T_{\rm eff}/{\rm K} = 4.60$, $\log L/L_\odot = 5.80$ on the H-R diagram. Top panels: Eddington ratios; ratios of radiative (purple) and convective (green) luminosity against Eddington luminosity. Here, radiative luminosity or convective luminosity refer to, respectively, the luminosity carried by radiative diffusion or convection. Unity is shown in a dashed black line, and the critical optical depth is indicated by a dashed red line (see text in Section 3.) Bottom panels: local opacity in each zone throughout the star (purple) and Eddington opacity (dashed black) $4\pi GcM/L$. Only locally super-Eddington radiative luminosity (in green) is considered in our eruptive mass-loss model.

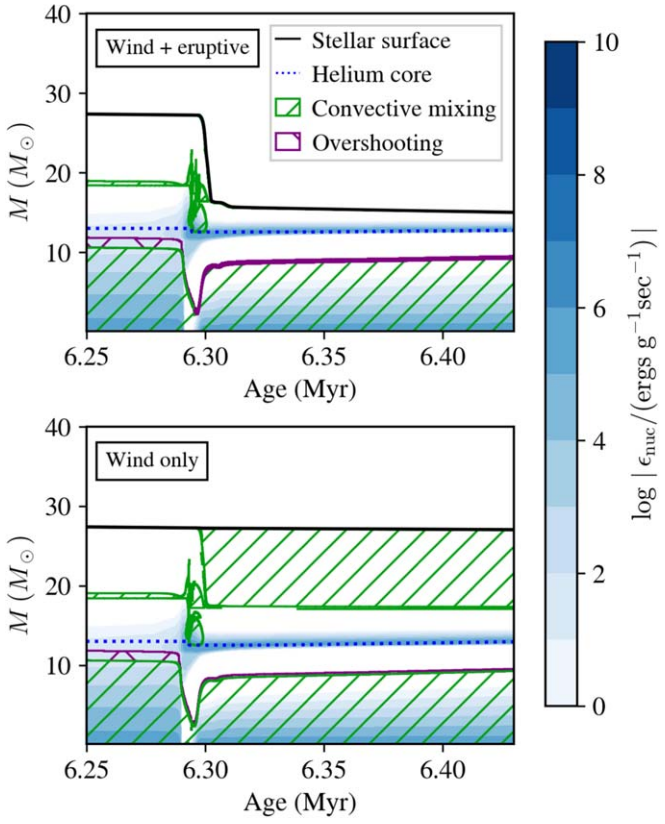

Figure 3. Kippenhahn diagram for $M_{\rm ZAMS} = 30\,M_\odot$, $Z = 1\,Z_\odot$ stars. The age x-axis focuses on the time of core He burning. This is the same model shown in Figure 1. Top panel: modeled with stellar wind and eruptive mass loss. Bottom panel: modeled only with stellar wind. Blue contours show the rate of nuclear energy generation, with the color bar on the right.

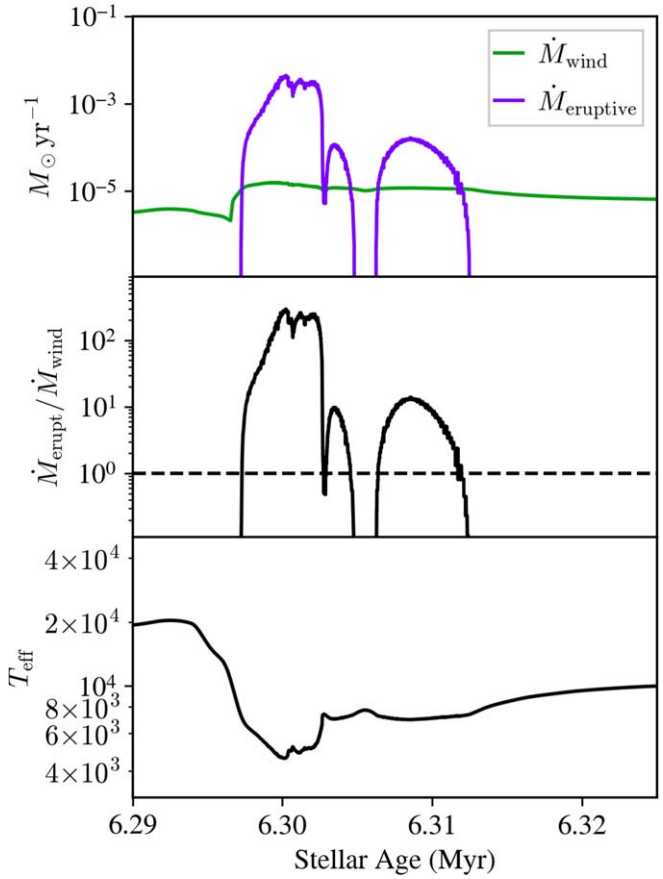

Figure 4. mass-loss rate, mass-loss ratio, and effective temperature over time of an $M_{\rm ZAMS} = 30\,M_\odot$ star with $\xi = 1.0$ and $Z = 1\,Z_\odot$. The middle panel shows the ratio between the mass-loss rate due to eruptive mass loss and the stellar wind mass-loss rate. The dashed black line marks when the ratio is unity.

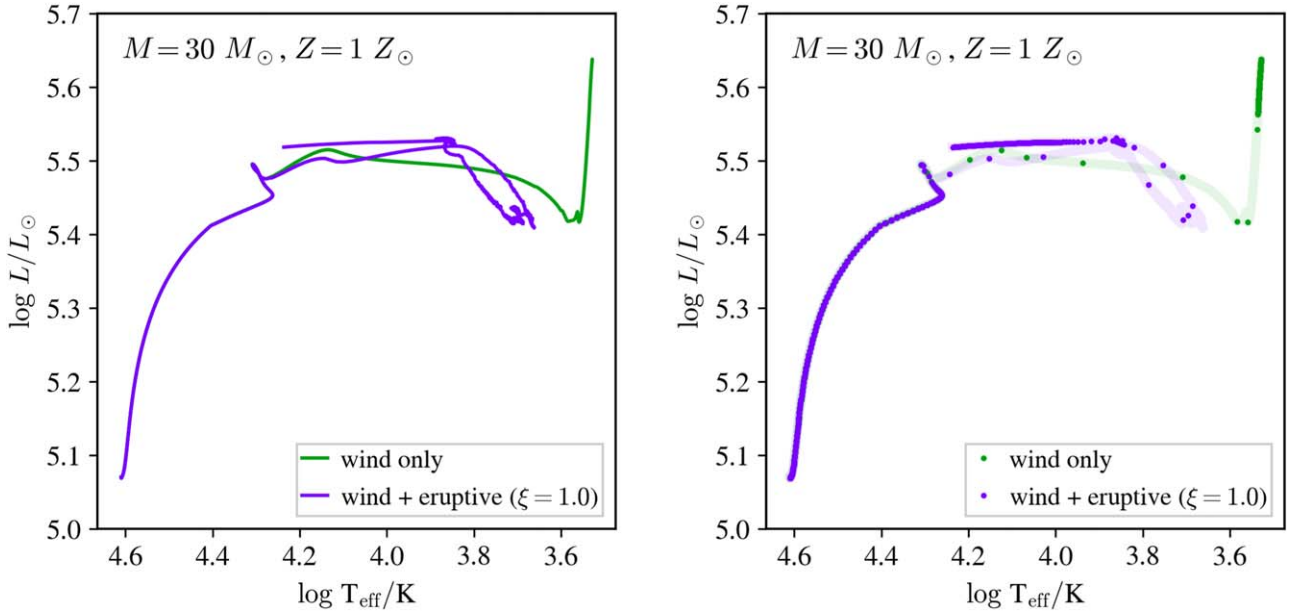

Figure 5. Evolutionary tracks of $M_{\rm ZAMS} = 30\,M_\odot$, $Z = 1\,Z_\odot$ stars. Left panel: H-R tracks for wind only (green) and eruptive mass loss + wind (purple) models. From the differing green and purple tracks, eruptive mass loss prevents evolution to the RSG phase. Right panel: evolutionary tracks sampled to one model every 1000 yr to show where stars are expected to be observed.

to become an RSG. The left panel of Figure 5 compares models run with (purple) and without (green) eruptive mass loss in addition to stellar winds. The right panel of Figure 5 samples the evolutionary track every 1000 yr, which allows better correspondence to where we expect stars to be observed. Based on this, we can see that the star modeled with eruptive mass loss is likely to be observed as a blue supergiant (BSG), whereas the star modeled with only stellar winds is likely to be observed as an RSG. Additionally, these sampled tracks capture how the star evolves across the Hertzsprung gap very rapidly in ∼10,000 yr. We note that our results are not sensitive to the choice of the RSG wind model since eruptive mass loss prevents evolution to the low temperatures applicable to RSG wind models.

We present our full mass-loss results for our $10-100\,M_\odot$ stars at $Z = 1\,Z_\odot$ in the top panels of Figure 6, which shows the evolution tracks of stars that span the full mass range on an H-R diagram. The mass-loss rate due to eruptive mass loss is colored in yellow, green, and blue contours. We take particular note that significant mass loss (green and blue contours) occurs in a vertical band between $3.5 < \log(T_{\rm eff}/{\rm K}) < 4.0$ as the stars evolve past the main sequence toward the RSG phase. Most of these models experiencing eruptive mass loss retain a surface hydrogen mass fraction between 0.25 and 0.5, with surface helium and nitrogen mass fractions between 0.5−0.75 and $1-1.8\times10^{-3,}$ respectively. The mass loss in this band is caused by the opacity peak in the stellar envelope due to both hydrogen and helium ionization transitions, as shown in Figure 2, where the peaks in Eddington ratios coincide with the hydrogen/helium opacity peak at $\sim10^4$ K (see discussion in Y.-F. Jiang et al. 2018). This result agrees with the 3D models in Y.-F. Jiang et al. (2018) where helium opacity peaks in the envelope of massive stars were found to drive mass loss.

Comparing the left and right panels in Figure 6, we see that while all the stars evolved with $\xi = 0.1$ (left column) evolve to become RSGs, stars with mass $\gtrsim 20\,M_\odot$ evolved with $\xi = 1.0$ (right column) do not become RSGs. This indicates that the presence of eruptive mass loss significantly alters the evolution of stars with mass $>20\,M_\odot$, suggesting that eruptive mass loss may be a physical mechanism behind the lack of RSGs above $20-30\,M_\odot$ as proposed by P. Massey et al. (2000), A. Heger et al. (2003), E. M. Levesque et al. (2009), S. Ekström et al. (2012) and the excess of BSGs (E. P. Bellinger et al. 2023). We show the change in the evolutionary tracks of our stars modeled with eruptive mass loss compared to those modeled only with stellar wind in Figure 7. From the top right panel of Figure 7, we confirm that for $M_{\rm ZAMS} \gtrsim 20\,M_\odot$, models evolved with eruptive mass loss at $\xi = 1.0$ do not evolve to temperatures cooler than $\log(T_{\rm eff}/{\rm K}) \approx 3.65$ and therefore do not become RSGs.

Additionally, for stars with initial masses greater than $50\,M_\odot$, some mass loss of order $10^{-5}\,M_\odot{\rm yr}^{-1}$ at higher $\log(T_{\rm eff}/{\rm K}) > 4.5$ K is predicted by our eruptive mass-loss model (seen in the top left of Figure 6). This is due to the iron opacity peak in the stellar envelope at $\sim1.8\times10^5$ K (B. Paxton et al. 2013; Y.-F. Jiang et al. 2015, see Figure 2), and follows the results from 3D models in Y.-F. Jiang et al. (2015). However, mass loss in the $\log(T_{\rm eff}/{\rm K}) > 4.5$ region is dominated by stellar winds rather than eruptive mass loss. This can be seen in Figure 8, which shows the fractional increase in overall mass loss due to eruptive mass loss (total mass loss/wind mass loss). Regions in the H-R diagram in which eruptive mass loss dominates substantially over stellar winds are marked in blue, which only occurs at lower temperatures. Therefore, from Figure 8, we determine that our eruptive mass loss is dominant over stellar winds in the $3.5 < \log(T_{\rm eff}/{\rm K}) < 4.0$ vertical band region.

Similarly, as shown in the bottom panels in Figures 6–8, a lower metallicity of $Z = 0.2\,Z_\odot \approx Z_{\rm SMC}$ also predicts a lack of RSGs above $\sim20\,M_\odot$ at $\xi = 1.0$. Since lower metallicities lead to lower opacities, increasing $L_{\rm Edd}$ and thereby reducing $\Gamma_{\rm Edd,\,rad} = L_{\rm rad}/L_{\rm Edd}$, some of the numerical challenges involving locally super-Eddington regions in the star (see Section 2) are avoided and the high-mass $Z = 0.2\,Z_\odot \approx Z_{\rm SMC}$ models are

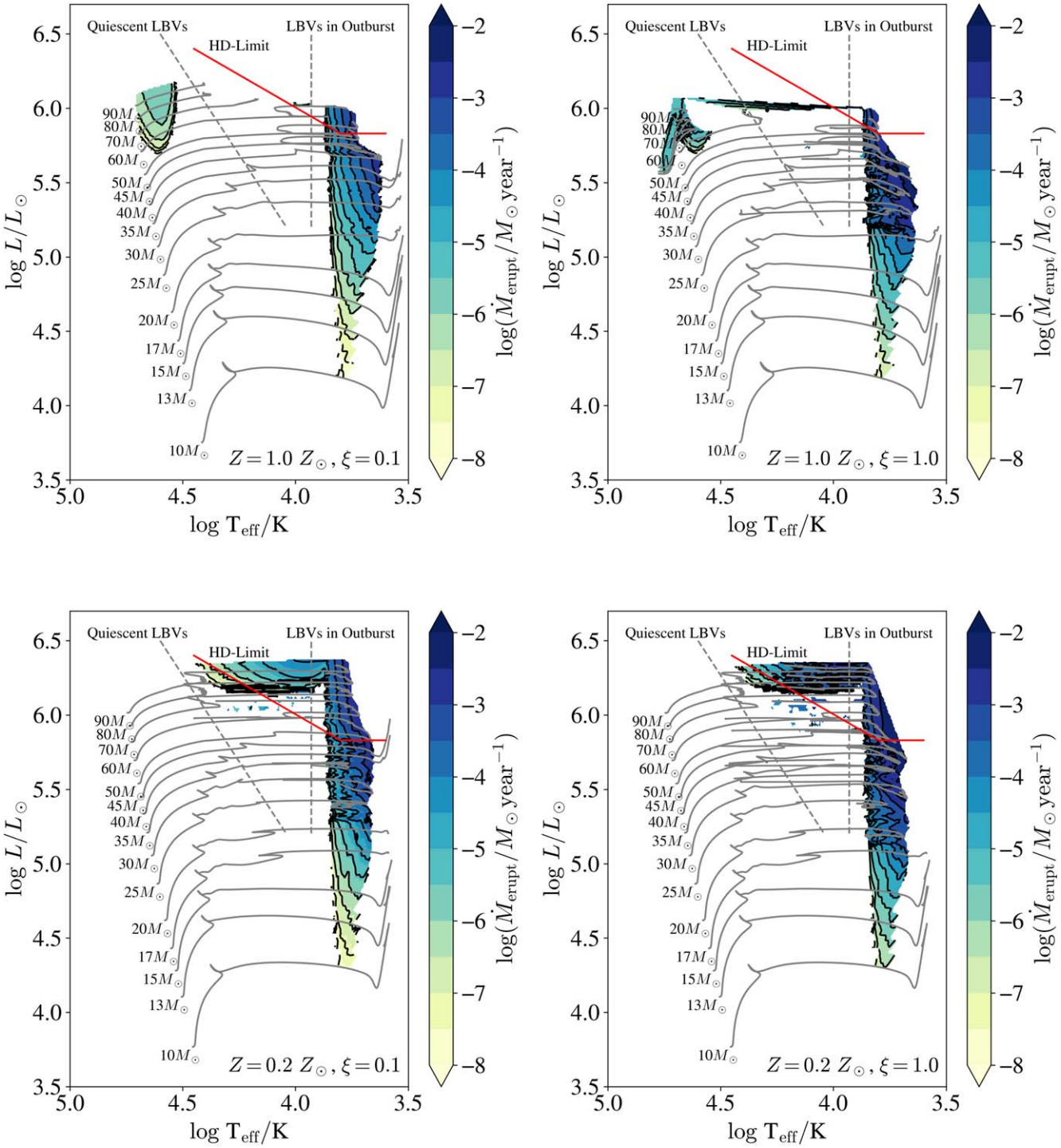

Figure 6. Eruptive mass-loss rates across the H-R diagram. Left column: $\xi = 0.1$. Right column: $\xi = 1.0$. Top row: $Z = 1\ Z_{\odot}$. Bottom row: $Z = Z_{\rm SMC} = 0.2\ Z_{\odot}$. Gray lines show the evolutionary tracks of stars from the beginning of main sequence until the end of the model run. Models were run at every 1 $M_{\odot}$ increments but only selected models are shown here for clarity. Dashed gray lines show two empirical tracks of Quiescent LBVs and LBVs in Outburst for reference. Solid red lines show the Humphreys–Davidson limit for reference. Colored contours show the rate of eruptive mass loss experienced by the star, with legend on the right.

able to evolve further than those with $Z = 1\ Z_{\odot}$. The lower panels of Figure 6 shows that at both metallicities, stars evolved with $\xi = 1.0$ exhibit higher rates of eruptive mass loss of up to $\sim 10^{-2} M_{\odot}\,{\rm yr}^{-1}$, whereas those evolved with $\xi = 0.1$ feature correspondingly lower mass-loss rates of up to $\sim 10^{-3} M_{\odot}\,{\rm yr}^{-1}$. Unsurprisingly, the region above the Humphreys–Davidson (HD) limit exhibits high levels of eruptive mass loss, as this observational limit corresponds to regions on the H-R diagram where surface stellar luminosities transition to become super-Eddington. Additionally, this region above the HD limit also exceeds the de Jager limit (C. de Jager 1984), wherein supersonic turbulent motions in the photosphere may have a destabilizing effect. Models at $Z = 1\ Z_{\odot}$ exhibited higher maximum eruptive mass-loss rates

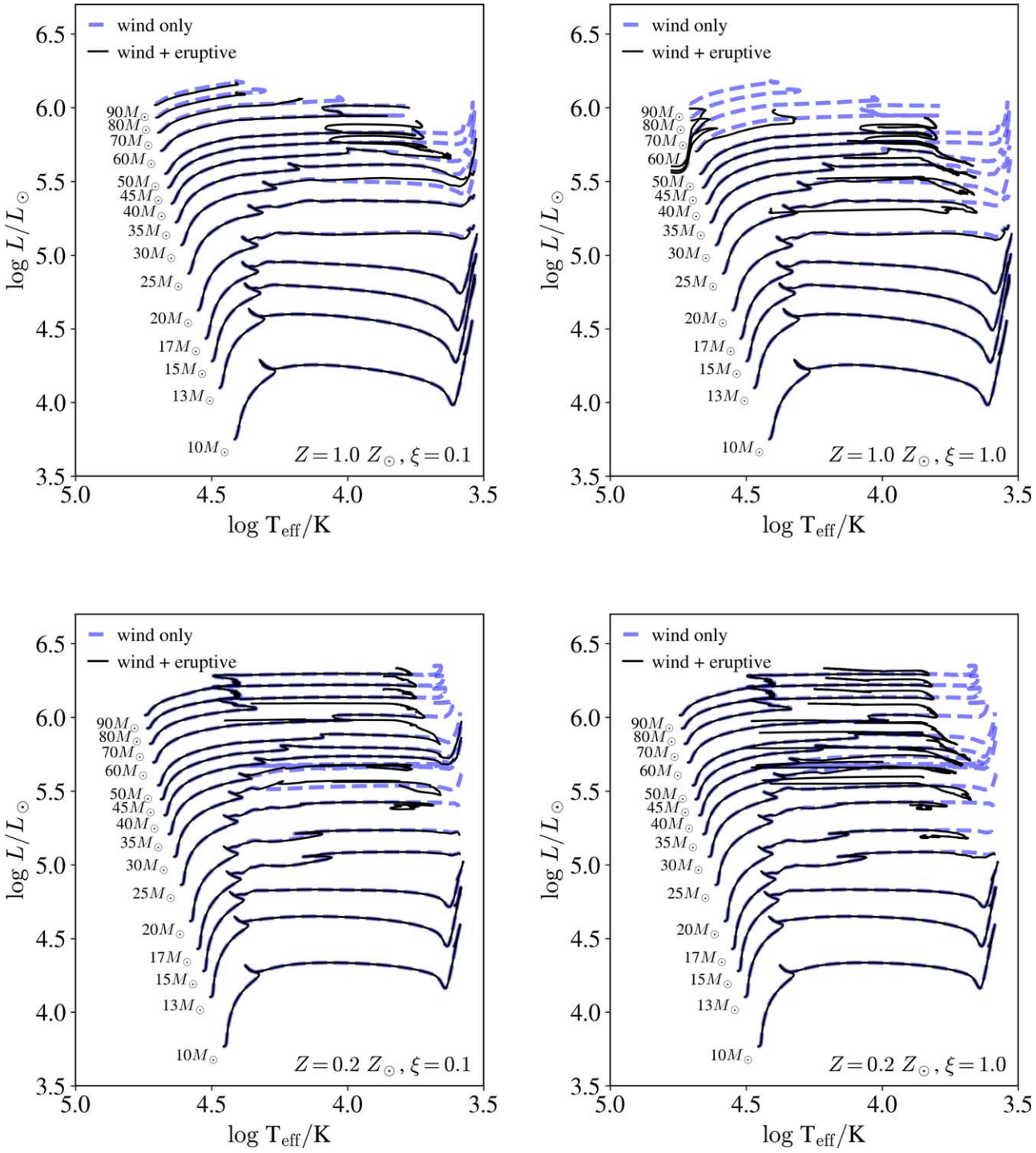

Figure 7. Evolutionary tracks of models with and without eruptive mass loss. Left column: $\xi = 0.1$. Right column: $\xi = 1.0$. First row: $Z = 1\ Z_\odot$. Second row: $Z = Z_{SMC} = 0.2\ Z_\odot$. All axes and labels follow Figure 6.

by up to an order of magnitude than those at $Z = 0.2\ Z_\odot$ for $M < 40\ M_\odot$. For $M > 40\ M_\odot$, the $Z = 0.2\ Z_\odot$ models were able to evolve further and therefore exhibited higher maximum eruptive mass-loss rates by at least an order of magnitude compared to $Z = 1\ Z_\odot$ models. The maximum eruptive mass-loss rate across all models is $\approx 3 \times 10^{-2}\ M_\odot\ \mathrm{yr}^{-1}$ (occurring for $\xi = 1.0$), which is consistent with observations (see Section 1).

5. Discussion and Conclusions

We studied eruptive mass loss in massive stars of varying masses (between 10 and 100 $M_\odot$) at two different metallicities ($Z_{SMC} \approx 0.2\ Z_\odot$ and $1\ Z_\odot$) with an implementation of an energy-based eruptive mass-loss model in the stellar evolution code MESA. Our model's mass-loss rate is determined by

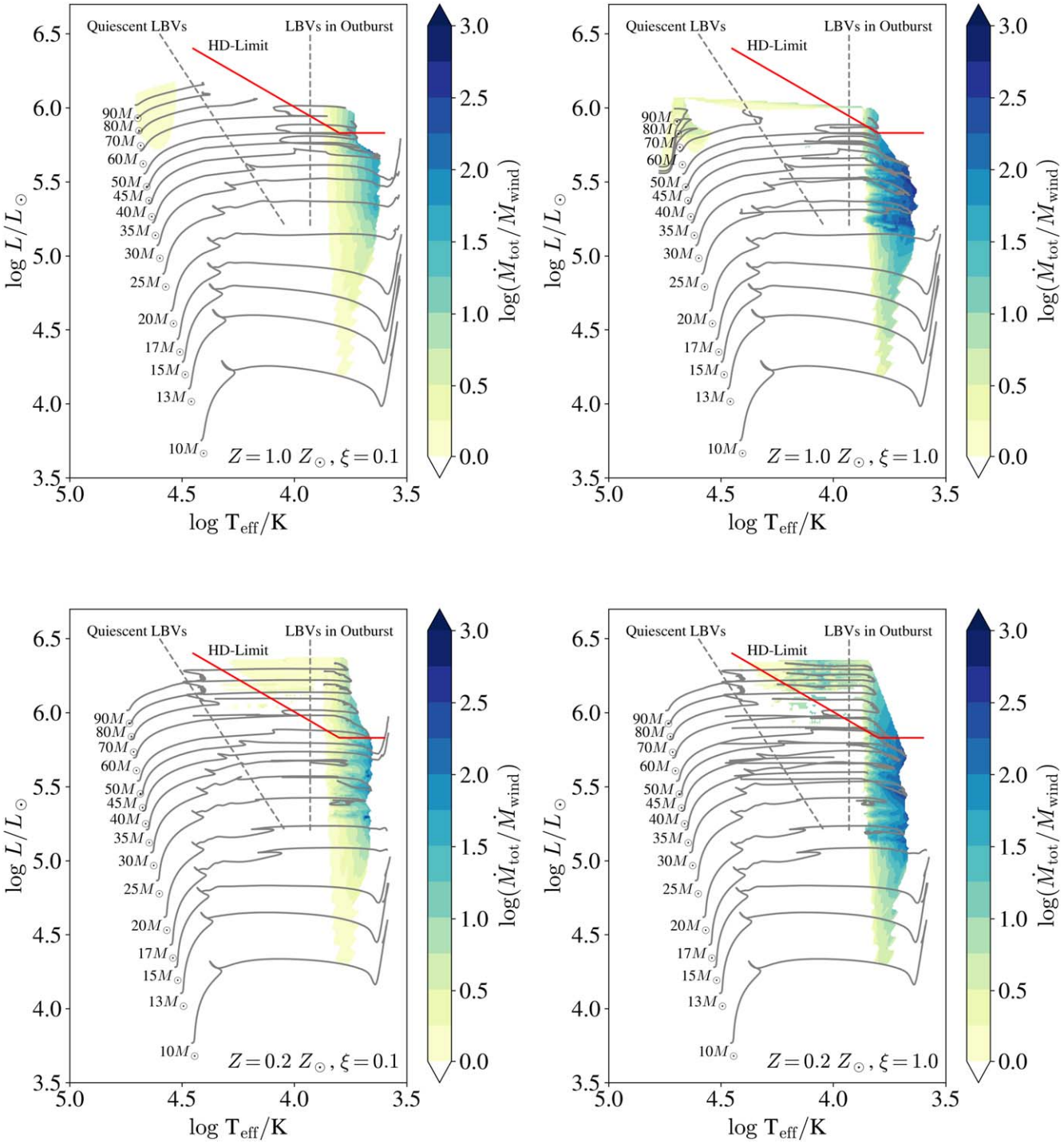

Figure 8. Ratio of total mass loss against wind mass-loss rates across the H-R diagram. Left column: $\xi = 0.1$. Right column: $\xi = 1.0$. Top row: $Z = 1\ Z_\odot$. Bottom row: $Z = Z_{\rm SMC} = 0.2\ Z_\odot$. Colored contours here show the ratio between total mass loss and wind mass loss, with legend on the right. Cooler colors (blues) indicate that eruptive mass loss is more dominant over stellar wind. All axes, labels, and other lines follow Figure 6.

considering photon diffusion through regions in the outer stellar envelope of these massive stars. As parts of the outer envelope may be locally super-Eddington, the excess (above Eddington) energy output from radiation may act on the fluid mass faster than dynamical, convective, and acoustic processes and exceed the binding energy of the overlaying layers, leading to mass loss.

We find that, at $\xi = 1.0$ (a model efficiency of 1.0 for the eruptive mass loss) and at both metallicity choices, stars with initial masses greater than $20\,M_\odot$ no longer evolve to become RSGs. This suggests that eruptive mass loss could be a physical mechanism that contributes to the observed lack of RSGs above $20-30\,M_\odot$, despite recent careful work determining relatively low mass-loss rates in well-characterized isolated RSGs (E. R. Beasor et al. 2020, 2023; L. Decin et al. 2024).

Alternative explanations other than eruptive mass loss for the lack of RSGs above $20-30\,M_\odot$ include envelope inflation (e.g., D. Sanyal et al. 2015, 2017) and binary interactions (e.g.,

N. Smith 2014; V. Morozova et al. 2015; R. Margutti et al. 2017). In the case of envelope inflation, D. Sanyal et al. (2015) ran 1D hydrodynamic stellar evolution models on core hydrogen burning massive stars and found that stars with initial mass $M > 40\,M_{\odot}$ locally exceeded the Eddington limit in the partial ionization zones of iron, helium, or hydrogen. The stars featured density inversions in their envelopes and experienced an increase of radius of up to a factor of $\sim$40, which alters the temperature and density structure such that envelope opacity decreases until the Eddington limit is no longer exceeded. While the authors found that the inflated envelopes remained bound, they noted that their models may have overestimated convective energy transport due to their implementation of MLT (therefore reducing $L_{\rm rad}$) and that multidimensional hydrodynamical simulations are needed to fully determine the stability of density inversions in stellar envelopes. Additionally, the authors speculatively mentioned that eruptions are a possible consequence of their very coolest models. Alternatively, binary interactions such as envelope stripping can lead to the formation of Wolf–Rayet stars that may never enter the RSG phase (e.g., L. M. Dray & C. A. Tout 2003; G. Meynet et al. 2011; G. Gräfener et al. 2012). However, mass-transferring binaries leave behind accretors and mergers, many of which are expected to evolve to the RSG phase (e.g., P. Podsiadlowski et al. 1993; G. Aldering et al. 1994; J. R. Maund et al. 2004; J. S. W. Claeys et al. 2011; S.-C. Yoon et al. 2017; F. R. N. Schneider et al. 2020; M. Renzo & Y. Götberg 2021; M. Renzo et al. 2023).

Additionally, our work may offer a possible solution to the "blue supergiant problem" wherein many BSGs having been observed despite the expectation of rapid evolution through the BSG phase. BSGs are hot, luminous stars with luminosities up to $\log(L/L_{\odot}) \approx 6.0$ and temperatures up to $\log(T_{\rm eff})/{\rm K} \approx 4.4$ (e.g., HD 5980 by E. C. Pickering & W. P. Fleming 1901; A. J. Cannon & E. C. Pickering 1918; G. Koenigsberger et al. 2010). It is generally thought that BSGs are either due to changes in stellar structure via mixing during evolution across the Hertzsprung gap (e.g., I. Iben 1993; D. Sugimoto & M. Y. Fujimoto 2000; S. E. de Mink et al. 2009, 2013; A. Schootemeijer et al. 2019), or post-main-sequence interactions such as mass transfer or mergers (e.g., P. Podsiadlowski et al. 1992; H. Braun & N. Langer 1995; S. E. de Mink et al. 2014; S. Justham et al. 2014). The eruptive mass loss presented in this work can be regarded as a possible intrinsic post-main-sequence behavior that may contribute to the formation of BSGs.

The energy-based model for eruptive mass loss presented in this work draws parallels with the "geyser model" presented in A. Maeder (1992). In this model, the mass-loss rate during a shell ejection event in a massive star is estimated by assuming the mass above super-Eddington peaks is ejected and accounting for the inward movement of these peaks at the local thermal timescale. Our model does not explicitly account for this effect since it would operate at timescales shorter than our code time step. As such, the geyser model may further enhance eruptive mass loss, though our model may approximately account for an average of such effects.

We emphasize that due to the numerical challenges of modeling massive stars in 1D (see Section 2), our models were only evolved far enough into core helium burning to probe the rightmost section of the H-R diagram where RSGs are found. Nevertheless, our work demonstrates that a physically motivated energy-based mass-loss model can adequately describe eruptive mass loss in massive stars. Additionally, we note that our work here treated the mass-loss model's efficiency factor ξ as a free parameter and explored the implications of $\xi = 1.0$ and $\xi = 0.1$. An observational study aimed at tuning this efficiency factor using LBV mass-loss observations will be conducted in future work.

Acknowledgments

S.J.C. and C.C. acknowledge support from NSF grant AST-131576. The Flatiron Institute is supported by the Simons Foundation.

Appendix

For RSG winds, we choose to adopt L. Decin et al. (2024) rather than one of the schemes included in `MESA`'s `Dutch` prescription (e.g., C. de Jager et al. 1988; H. Nieuwenhuijzen & C. de Jager 1990) for which mass-loss rates are overestimated (see Section 1). While doing so alters stellar evolution in the RSG phase, it does not affect our eruptive mass-loss result: Figure 9 compares models run with L. Decin et al. (2024) and with C. de Jager et al. (1988) mass loss for $T_{\rm eff} < 4000$ K. The L. Decin et al. (2024) winds only affect the very late RSG phase, and does not impact the model with eruptive wind in the case shown (in purple) since such models do not evolve cool enough to enter the L. Decin et al. (2024) regime. We note that although L. Decin et al. (2024) produces mass-loss rates calibrated to careful observations in well-characterized individual stellar populations (in broad agreement with E. R. Beasor et al. 2023's correction to the E. R. Beasor et al. 2020 rates), it contains in it a dependence on the initial mass of stars as estimated from cluster characteristics, which need not

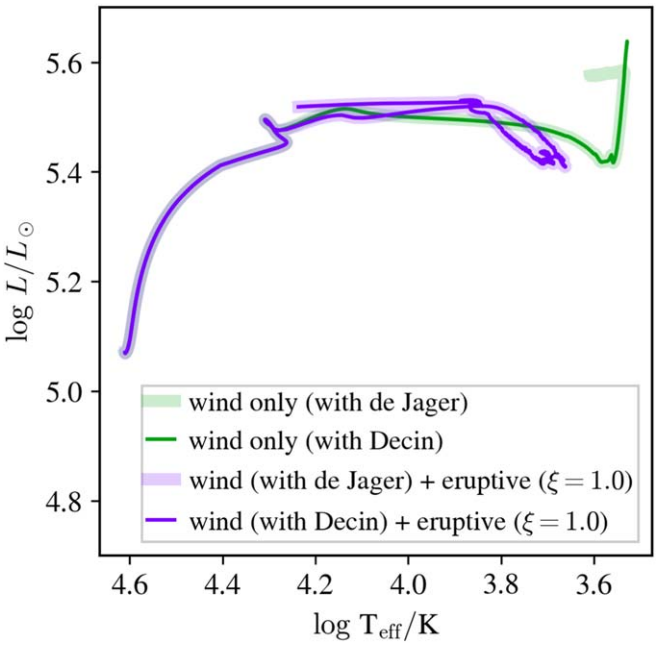

Figure 9. Evolutionary tracks of $M_{\rm ZAMS} = 30\,M_{\odot}$, $Z = 1\,Z_{\odot}$ stars. H-R tracks for wind only (green) and eruptive mass-loss + wind (purple) models. The models marked with "Decin" contain the modification described in Section 3, while those using the old C. de Jager et al. (1988) rates are marked with "de Jager." From the differing green and purple tracks, eruptive mass loss prevents evolution to RSG phase.

correspond to the initial mass of a stellar model in MESA. A more proper treatment correcting for this when comparing models to stellar populations might include a variable scaling factor akin to the dutch_scaling_factor for the Dutch stellar wind prescription.

ORCID iDs

Shelley J. Cheng https://orcid.org/0000-0002-5462-0294
Jared A. Goldberg https://orcid.org/0000-0003-1012-3031
Matteo Cantiello https://orcid.org/0000-0002-8171-8596
Evan B. Bauer https://orcid.org/0000-0002-4791-6724
Mathieu Renzo https://orcid.org/0000-0002-6718-9472
Charlie Conroy https://orcid.org/0000-0002-1590-8551

References

Aldering, G., Humphreys, R. M., & Richmond, M. 1994, AJ, 107, 662
Angulo, C., Arnould, M., Rayet, M., et al. 1999, NuPhA, 656, 3
Asplund, M., Amarsi, A. M., & Grevesse, N. 2021, A&A, 653, A141
Banerjee, S., Belczynski, K., Fryer, C. L., et al. 2020, A&A, 639, A41
Beasor, E. R., & Davies, B. 2018, MNRAS, 475, 55
Beasor, E. R., Davies, B., Smith, N., et al. 2020, MNRAS, 492, 5994
Beasor, E. R., Davies, B., Smith, N., et al. 2023, MNRAS, 524, 2460
Belczynski, K., Bulik, T., Fryer, C. L., et al. 2010, ApJ, 714, 1217
Bellinger, E. P., de Mink, S. E., van Rossem, W. E., & Justham, S. 2024, ApJL, 967, L39
Blaes, O., & Socrates, A. 2003, ApJ, 596, 509
Böhm-Vitense, E. 1958, ZA, 46, 108
Braun, H., & Langer, N. 1995, A&A, 297, 483
Bruch, R. J., Gal-Yam, A., Yaron, O., et al. 2023, ApJ, 952, 119
Cannon, A. J., & Pickering, E. C. 1918, AnHar, 91, 1
Cassisi, S., Potekhin, A. Y., Pietrinferni, A., Catelan, M., & Salaris, M. 2007, ApJ, 661, 1094
Castor, J. I., Abbott, D. C., & Klein, R. I. 1975, ApJ, 195, 157
Ceverino, D., & Klypin, A. 2009, ApJ, 695, 292
Chiavassa, A., Kravchenko, K., & Goldberg, J. A. 2024, LRCA, 10, 2
Chugunov, A. I., Dewitt, H. E., & Yakovlev, D. G. 2007, PhRvD, 76, 025028
Claeys, J. S. W., de Mink, S. E., Pols, O. R., Eldridge, J. J., & Baes, M. 2011, A&A, 528, A131
Cox, J. P., & Giuli, R. T. 1968, Principles of Stellar Structure (New York: Gordon and Breach)
Crowther, P. A., Hillier, D. J., Evans, C. J., et al. 2002, ApJ, 579, 774
Cure, M., & Araya, I. 2023, Galax, 11, 68
Cyburt, R. H., Amthor, A. M., Ferguson, R., et al. 2010, ApJS, 189, 240
Decin, L., Richards, A. M. S., Marchant, P., & Sana, H. 2024, A&A, 681, A17
de Jager, C. 1984, A&A, 138, 246
de Jager, C., Nieuwenhuijzen, H., & van der Hucht, K. A. 1988, A&AS, 72, 259
de Mink, S. E., Cantiello, M., Langer, N., et al. 2009, A&A, 497, 243
de Mink, S. E., Langer, N., Izzard, R. G., Sana, H., & de Koter, A. 2013, ApJ, 764, 166
de Mink, S. E., Sana, H., Langer, N., Izzard, R. G., & Schneider, F. R. N. 2014, ApJ, 782, 7
Dessart, L., Hillier, D. J., Waldman, R., & Livne, E. 2013, MNRAS, 433, 1745
Dominik, M., Belczynski, K., Fryer, C., et al. 2012, ApJ, 759, 52
Dorn-Wallenstein, T. Z., Neugent, K. F., & Levesque, E. M. 2023, ApJ, 959, 102
Dray, L. M., & Tout, C. A. 2003, MNRAS, 341, 299
Ekström, S., Georgy, C., Eggenberger, P., et al. 2012, A&A, 537, A146
Evans, C. J., Crowther, P. A., Fullerton, A. W., & Hillier, D. J. 2004, ApJ, 610, 1021
Ferguson, J. W., Alexander, D. R., Allard, F., et al. 2005, ApJ, 623, 585
Fields, C. E., & Couch, S. M. 2021, ApJ, 921, 28
Figer, D. F., Najarro, F., Gilmore, D., et al. 2002, ApJ, 581, 258
Fragos, T., Andrews, J. J., Bavera, S. S., et al. 2023, ApJS, 264, 45
Fuller, G. M., Fowler, W. A., & Newman, M. J. 1985, ApJ, 293, 1
Fullerton, A. W., Massa, D. L., & Prinja, R. K. 2006, ApJ, 637, 1025
Geen, S., Rosdahl, J., Blaizot, J., Devriendt, J., & Slyz, A. 2015, MNRAS, 448, 3248
Georgy, C., Ekström, S., Meynet, G., et al. 2012, A&A, 542, A29
Glebbeek, E., Gaburov, E., de Mink, S. E., Pols, O. R., & Portegies Zwart, S. F. 2009, A&A, 497, 255
Goldberg, J. A., Jiang, Y.-F., & Bildsten, L. 2022, ApJ, 929, 156
Goldman, S. R., van Loon, J. T., Zijlstra, A. A., et al. 2017, MNRAS, 465, 403
Gräfener, G., Vink, J. S., Harries, T. J., & Langer, N. 2012, A&A, 547, A83
Grevesse, N., & Sauval, A. J. 1998, SSRv, 85, 161
Heckman, T. M., Armus, L., & Miley, G. K. 1990, ApJS, 74, 833
Heger, A., Fryer, C. L., Woosley, S. E., Langer, N., & Hartmann, D. H. 2003, ApJ, 591, 288
Herwig, F. 2000, A&A, 360, 952
Hillier, D. J., Lanz, T., Heap, S. R., et al. 2003, ApJ, 588, 1039
Houdek, G., & Gough, D. O. 2011, MNRAS, 418, 1217
Humphreys, R. M., & Davidson, K. 1984, Sci, 223, 243
Humphreys, R. M., & Davidson, K. 1994, PASP, 106, 1025
Iben, I. J. 1993, ApJ, 415, 767
Iglesias, C. A., & Rogers, F. J. 1993, ApJ, 412, 752
Iglesias, C. A., & Rogers, F. J. 1996, ApJ, 464, 943
Irwin, A. W., 2004 The FreeEOS Code for Calculating the Equation of State for Stellar Interiors, Astrophysics Source Code Library, ascl:1211.002, http://freeeos.sourceforge.net/
Itoh, N., Hayashi, H., Nishikawa, A., & Kohyama, Y. 1996, ApJS, 102, 411
Jacobson-Galán, W. V., Dessart, L., Davis, K. W., et al. 2024, ApJ, 970, 189
Jermyn, A. S., Anders, E. H., Lecoanet, D., Cantiello, M., & Goldberg, J. A. 2022, RNAAS, 6, 29
Jermyn, A. S., Bauer, E. B., Schwab, J., et al. 2023, ApJS, 265, 15
Jermyn, A. S., Schwab, J., Bauer, E., Timmes, F. X., & Potekhin, A. Y. 2021, ApJ, 913, 72
Jiang, Y.-F., Cantiello, M., Bildsten, L., et al. 2018, Natur, 561, 498
Jiang, Y.-F., Cantiello, M., Bildsten, L., Quataert, E., & Blaes, O. 2015, ApJ, 813, 74
Johnston, C., Michielsen, M., Anders, E. H., et al. 2024, ApJ, 964, 170
Jones, S., Hirschi, R., Nomoto, K., et al. 2013, ApJ, 772, 150
Josiek, J., Ekström, S., & Sander, A. A. C. 2024, A&A, 688, A71
Joss, P. C., Salpeter, E. E., & Ostriker, J. P. 1973, ApJ, 181, 429
Justham, S., Podsiadlowski, P., & Vink, J. S. 2014, ApJ, 796, 121
Kiriakidis, M., Fricke, K. J., & Glatzel, W. 1993, MNRAS, 264, 50
Koenigsberger, G., Georgiev, L., Hillier, D. J., et al. 2010, AJ, 139, 2600
Kuhfuss, R. 1986, A&A, 160, 116
Lamers, H. J. G. L. M., & Cassinelli, J. P. 1999, Introduction to Stellar Winds (Cambridge: Cambridge Univ. Press)
Langanke, K., & Martınez-Pinedo, G. 2000, NuPhA, 673, 481
Levesque, E. M., Massey, P., Plez, B., & Olsen, K. A. G. 2009, AJ, 137, 4744
Li, Y., Chen, X.-h., & Chen, H.-l. 2019, ApJ, 870, 77
Liljegren, S., Höfner, S., Nowotny, W., & Eriksson, K. 2016, A&A, 589, A130
Maeder, A. 1992, in Instabilities in Evolved Super- and Hypergiants, ed. C. de Jager & H. Nieuwenhuijzen (Amsterdam: North-Holland), 138
Mapelli, M. 2016, MmSAI, 87, 567
Margutti, R., Kamble, A., Milisavljevic, D., et al. 2017, ApJ, 835, 140
Massa, D., Fullerton, A. W., Sonneborn, G., & Hutchings, J. B. 2003, ApJ, 586, 996
Massey, P., Waterhouse, E., & DeGioia-Eastwood, K. 2000, AJ, 119, 2214
Maund, J. R., Smartt, S. J., Kudritzki, R. P., Podsiadlowski, P., & Gilmore, G. F. 2004, Natur, 427, 129
Mauron, N., & Josselin, E. 2011, A&A, 526, A156
Meynet, G., Chomienne, V., Ekström, S., et al. 2015, A&A, 575, A60
Meynet, G., Georgy, C., Hirschi, R., et al. 2011, BSRSL, 80, 266
Meynet, G., & Maeder, A. 2003, A&A, 404, 975
Moriya, T. J., & Yoon, S.-C. 2022, MNRAS, 513, 5606
Morozova, V., Piro, A. L., Renzo, M., et al. 2015, ApJ, 814, 63
Morozova, V., Piro, A. L., & Valenti, S. 2017, ApJ, 838, 28
Nieuwenhuijzen, H., & de Jager, C. 1990, A&A, 231, 134
Nugis, T., & Lamers, H. J. G. L. M. 2000, A&A, 360, 227
Oda, T., Hino, M., Muto, K., Takahara, M., & Sato, K. 1994, ADNDT, 56, 231
Owocki, S. P., Castor, J. I., & Rybicki, G. B. 1988, ApJ, 335, 914
Owocki, S. P., Gayley, K. G., & Shaviv, N. J. 2004, ApJ, 616, 525
Pastorello, A., Smartt, S. J., Mattila, S., et al. 2007, Natur, 447, 829
Paxton, B., Bildsten, L., Dotter, A., et al. 2011, ApJS, 192, 3
Paxton, B., Cantiello, M., Arras, P., et al. 2013, ApJS, 208, 4
Paxton, B., Marchant, P., Schwab, J., et al. 2015, ApJS, 220, 15
Paxton, B., Schwab, J., Bauer, E. B., et al. 2018, ApJS, 234, 34
Paxton, B., Smolec, R., Schwab, J., et al. 2019, ApJS, 243, 10
Pereira, A. W., Janot-Pacheco, E., Emilio, M., et al. 2024, A&A, 686, A20
Pickering, E. C., & Fleming, W. P. 1901, ApJ, 14, 144
Podsiadlowski, P., Hsu, J. J. L., Joss, P. C., & Ross, R. R. 1993, Natur, 364, 509

Podsiadlowski, P., Joss, P. C., & Hsu, J. J. L. 1992, ApJ, 391, 246
Potekhin, A. Y., & Chabrier, G. 2010, CoPP, 50, 82
Poutanen, J. 2017, ApJ, 835, 119
Prendergast, K. H., & Spiegel, E. A. 1973, CoASP, 5, 43
Puls, J., Markova, N., Scuderi, S., et al. 2006, A&A, 454, 625
Puls, J., Vink, J. S., & Najarro, F. 2008, A&ARv, 16, 209
Renzo, M., & Götberg, Y. 2021, ApJ, 923, 277
Renzo, M., Ott, C. D., Shore, S. N., & de Mink, S. E. 2017, A&A, 603, A118
Renzo, M., Zapartas, E., Justham, S., et al. 2023, ApJL, 942, L32
Rogers, F. J., & Nayfonov, A. 2002, ApJ, 576, 1064
Sanyal, D., Grassitelli, L., Langer, N., & Bestenlehner, J. M. 2015, A&A, 580, A20
Sanyal, D., Langer, N., Szécsi, D., C Yoon, S., & Grassitelli, L. 2017, A&A, 597, A71
Saumon, D., Chabrier, G., & van Horn, H. M. 1995, ApJS, 99, 713
Schlegel, E. M. 1990, MNRAS, 244, 269
Schneider, F. R. N., Ohlmann, S. T., Podsiadlowski, P., et al. 2020, MNRAS, 495, 2796
Schootemeijer, A., Langer, N., Grin, N. J., & Wang, C. 2019, A&A, 625, A132
Schootemeijer, A., Shenar, T., Langer, N., et al. 2024, A&A, 689, A157
Schultz, W. C., Bildsten, L., & Jiang, Y.-F. 2023, ApJL, 951, L42
Shiber, S., Chatzopoulos, E., Munson, B., & Frank, J. 2024, ApJ, 962, 168
Smith, N. 2014, ARA&A, 52, 487
Smith, N. 2017, RSPTA, 375, 20160268
Smith, N., & Owocki, S. P. 2006, ApJL, 645, L45
Steinwandel, U. P., & Goldberg, J. A. 2023, arXiv:2310.11495
Suárez-Madrigal, A., Krumholz, M., & Ramirez-Ruiz, E. 2013, arXiv:1304.2317
Sugimoto, D., & Fujimoto, M. Y. 2000, ApJ, 538, 837
Tacconi, L. J., Genzel, R., & Sternberg, A. 2020, ARA&A, 58, 157
Timmes, F. X. 1999, ApJS, 124, 241
Timmes, F. X., & Swesty, F. D. 2000, ApJS, 126, 501
Trampedach, R., & Stein, R. F. 2011, ApJ, 731, 78
Uchida, H., Shibata, M., Takahashi, K., & Yoshida, T. 2019, PhRvD, 99, 041302
van Loon, J. T., Cioni, M. R. L., Zijlstra, A. A., & Loup, C. 2005, A&A, 438, 273
Vink, J. S., de Koter, A., & Lamers, H. J. G. L. M. 2001, A&A, 369, 574
Vink, J. S., Higgins, E. R., Sander, A. A. C., & Sabhahit, G. N. 2021, MNRAS, 504, 146
Vink, J. S., & Sabhahit, G. N. 2023, A&A, 678, L3
Willson, L. A. 2000, ARA&A, 38, 573
Wood, P. R., Bessell, M. S., & Fox, M. W. 1983, ApJ, 272, 99
Wood, P. R., Whiteoak, J. B., Hughes, S. M. G., et al. 1992, ApJ, 397, 552
Xin, C., Renzo, M., & Metzger, B. D. 2022, MNRAS, 516, 5816
Yoon, S.-C., Dessart, L., & Clocchiatti, A. 2017, ApJ, 840, 10
Ziosi, B. M., Mapelli, M., Branchesi, M., & Tormen, G. 2014, MNRAS, 441, 3703